small structures
www.small-structures.com

# 3D Temperature Mapping During Photothermal Therapy in Cellular Assemblies

*Joana F. Soeiro, Rute A. Pereira, Rui Oliveira-Silva, Filipa L. Sousa, Vítor M. Gaspar, João F. Mano, Ángel Millán, Claudia Innocenti, Manuel Mariani, Alessandro Lascialfari, and Nuno J. O. Silva**

**Control over temperature in three space dimensions and time is of utmost importance in many contexts, including photothermal therapies, where it is expected to provide valuable insights and enhance clinical outcomes. Current techniques for noncontact temperature mapping during hyperthermia are restricted to 2D imaging, due to the lack of strategies able to provide images in suitable time frames for the inevitable large amount of information encompassed in 3D tomography. Iron selenide nanoparticles (NPs) are developed with high temperature sensitivity that, in combination with low-field magnetic resonance imaging, enable 3D temperature imaging in the ≈20 s time frame. This approach is suitable for monitoring and evaluating photothermal therapy applied to cellular assemblies, which typically occurs over a time frame of tens of minutes. In addition, iron selenide NPs behave, simultaneously, as photothermal and thermometric agents embedded in cellular models at concentrations where their cytotoxicity is low. This dual functionality enables to control the depth achieved by the therapy with a temperature accuracy ≤1 °C, enabling the detection and control of hot spots that would be otherwise overlooked. Overall, this is a universal approach for temperature mapping in 3D and for localized heating in virtually any living tissue.**

## 1. Introduction

As the characteristic size of objects decreases across the microscale, contact thermometers are abandoned in favor of noncontact thermometers. Many of these noncontact thermometers are based on local probes and a device able to excite and detect a thermometric property of that probe (e.g., a temperature-dependent light intensity, wavelength, decay time, or magnetic signal). Despite great advances, noncontact thermometers collect temperature, at most, in two space dimensions.[1,2] In real systems, heat flows in 3D such that 2D noncontact thermometers give just a plane view of a 3D reality. Noncontact thermometers based on probes coupled to the detector system, such as atomic force-based ones, are intrinsically 2D. In contrast, nanothermometers based on decoupled probes could, in principle, be used for 3D temperature mapping. The first hurdle to 3D temperature mapping is the penetration of excitation stimulus down to the point under measurement and the exit of the signal. Optical temperature imaging has an excellent space resolution but it has intrinsic limitations for in-depth sensing, which prevents its application in many practical applications.[1,3] In contrast, magnetic temperature imaging has an excellent penetration depth but a small variation of contrast with temperature. This is the case of magnetic resonance imaging (MRI) thermometry, which is based on the intrinsic variation of contrast parameters with

J. F. Soeiro, R. A. Pereira, R. Oliveira-Silva, N. J. O. Silva
Department of Physics and CICECO - Aveiro Institute of Materials
University of Aveiro
Campus Universitário de Santiago, 3810-193 Aveiro, Portugal
E-mail: nunojoao@ua.pt

J. F. Soeiro, R. A. Pereira, R. Oliveira-Silva, F. L. Sousa, V. M. Gaspar, J. F. Mano, N. J. O. Silva
Department of Chemistry and CICECO - Aveiro Institute of Materials
University of Aveiro
Campus Universitário de Santiago, 3810-193 Aveiro, Portugal

The ORCID identification number(s) for the author(s) of this article can be found under https://doi.org/10.1002/sstr.202400658.



**DOI: 10.1002/sstr.202400658**

Á. Millán
Institute of Nanoscience and Materials of Aragon (INMA)
CSIC-University of Zaragoza
Zaragoza 50009, Spain

C. Innocenti
Dipartimento di Chimica
Università di Firenze and INSTM
50019 Sesto Fiorentino (FI), Italy

C. Innocenti
ICCOM-CNR
50019 Sesto Fiorentino (FI), Italy

M. Mariani, A. Lascialfari
Department of Physics
University of Pavia
27100 Pavia, Italy

A. Lascialfari
INFN, Istituto Nazionale di Fisica Nucleare
27100 Pavia, Italy

temperature, such as proton resonance frequency and longitudinal and transverse relaxation times.[4] This small variation of contrast with temperature results in the need for acquisition times incompatible with 3D temperature mapping. This is the second hurdle to achieve 3D temperature mapping: temperature is dynamic such that the total time spent in 3D scanning must be under the characteristic time of this dynamics. In MRI thermometry, larger contrast variations with temperature can be obtained with the use of contrast agents, such as millimetric piece of metallic gadolinium with a large variation of its ability to generate contrast around 18 °C, associated with a large variation of magnetization around that transition temperature.[5] Clearly, the practical application of a millimeter-sized probe is limited, and an improved version of this strategy using micrometric particles appeared later.[6] Anyway, it is quite difficult to make smaller (nanosized) metallic gadolinium particles, as they undergo spontaneous oxidation upon exposure to air ambient conditions,[7] and it is not clear how to increase their transition temperature from 18 to ≈42 °C, which is required for clinical applications. More recently, aggregated manganese, cobalt, and zinc ferrite nanocrystals appeared as an option, with the advantage of tuning the transition temperature by doping.[8–11] However, having simultaneously isolated nanoparticles (NPs) and a large temperature-response is proving difficult: in agglomerates of nanocrystals the decrease of magnetization with temperature is high, leading to a good temperature sensitivity, but when low-anisotropy isolated NPs are obtained, the decrease of magnetization is much smaller.[12] We hypothesized that the breakthrough into the 3rd dimension in temperature mapping would be possible by combining 1) high anisotropy nanosized magnetic systems, where a sharper decrease of magnetization is expected,[13] with 2) emergent MRI scanners with low-field, at which a sharper decrease of magnetization is preserved. Moreover, we envisage that in real clinical practice, the use of contrast agents to provide temperature maps must be carefully considered in terms of a risk/benefit balance. This balance is expected to increase dramatically toward the benefit side if the contrast agent is combined with a photothermal agent and hyperthermia is the therapy of choice. In such cases, the thermometric feature would be regarded as a great added value to an already needed clinical practice.

Here, we show isolated and functionalized NPs that combine low cytotoxicity, suitable efficiency in the 1st and 2nd windows of near-infrared (NIR) hyperthermia, and a high magnetic anisotropy granting an excellent thermometric response that can be imaged by low-field MRI scanners and provide 3D temperature maps in the temperature window used in clinical NIR hyperthermia (**Figure 1**). The combination of these three pillars 1) low

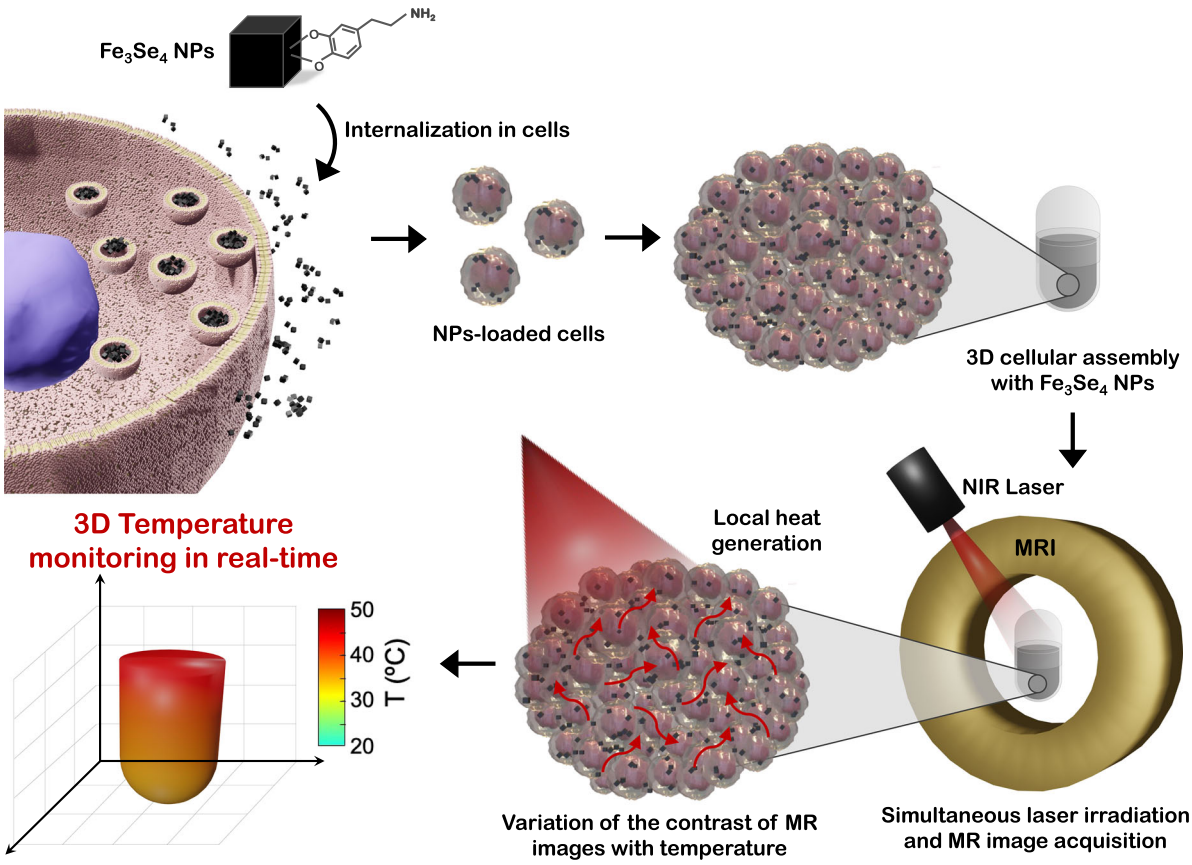


**Figure 1.** Schematic representation of the use of $Fe_3Se_4$ NPs with dopamine functionalization for local heat generation and 3D temperature monitoring by MRI thermometry during laser irradiation of 3D cellular assemblies.

cytotoxicity, 2) good photothermal efficiency, and 3) high-temperature sensitivity enabling 3D temperature mapping in isolated NPs is critical for a formulation able to eventually reach the market of photothermal-thermometric contrast agents.

## 2. Results and Discussion

The particles here reported are iron selenide ($Fe_3Se_4$) NPs with a rhombohedral shape and an average size of $177 \pm 16$ nm (**Figure 2**a,b and S2–S4, Supporting Information). The production of pure $Fe_3Se_4$ NPs requires a precise tuning of parameters such as temperature, temperature ramp, precursors, solvent, and stabilizing agents, since other phases ($FeSe_2$, $Fe_7Se_8$, and FeSe) may also nucleate and grow. Here, we explore the production of $Fe_3Se_4$ NPs using a simpler route, when compared to the current state-of-the-art.[14] The route here presented involves the use of iron acetate and selenium-octadecene as precursors, the use of octadecene as the solvent, tetradecylphosphonic acid and 1-Dodecanethiol as stabilizing agents, and the thermal decomposition of the precursors into the NPs at 250 °C with a heating ramp of 5 °C $min^{-1}$. Such a thermal decomposition route in organic media has the benefit of producing isolated and better controlled NPs and the drawback of having a hydrophobic surface, such that an extra phase-transfer step is needed for their use in cellular medium. To this aim, we explored the use of caffeic acid and dopamine, which are molecules with a catechol group that is expected to interact with the iron atoms located at the surface of the NPs, as previously found in $Fe_3Se_4$[14] and $Fe_3O_4$.[15] The final result is hydrophilic NPs with reactive amine or carboxyl groups, that can be explored as a photothermal and thermometric agent in cells.

As mentioned in the introduction, the first pillar on which a good photothermal-contrast agent stands is low cytotoxicity. This was accessed using the AlamarBlue assay up to 72 h after NPs were incubated with L929 mouse fibroblast cells. Cells remained viable (>85%) for all the time points tested for the incubation concentration range of 0–500 μg $mL^{-1}$ of NPs (Figure 2d and S5, Supporting Information). Consequently, it is possible to use incubation concentrations in this range for the remaining studies involving simultaneous NIR hyperthermia and MRI thermometry in 3D cellular assemblies. Afterward, an analysis of $Fe_3Se_4$ NPs internalization in monocultures of L929 cells was performed through confocal imaging,

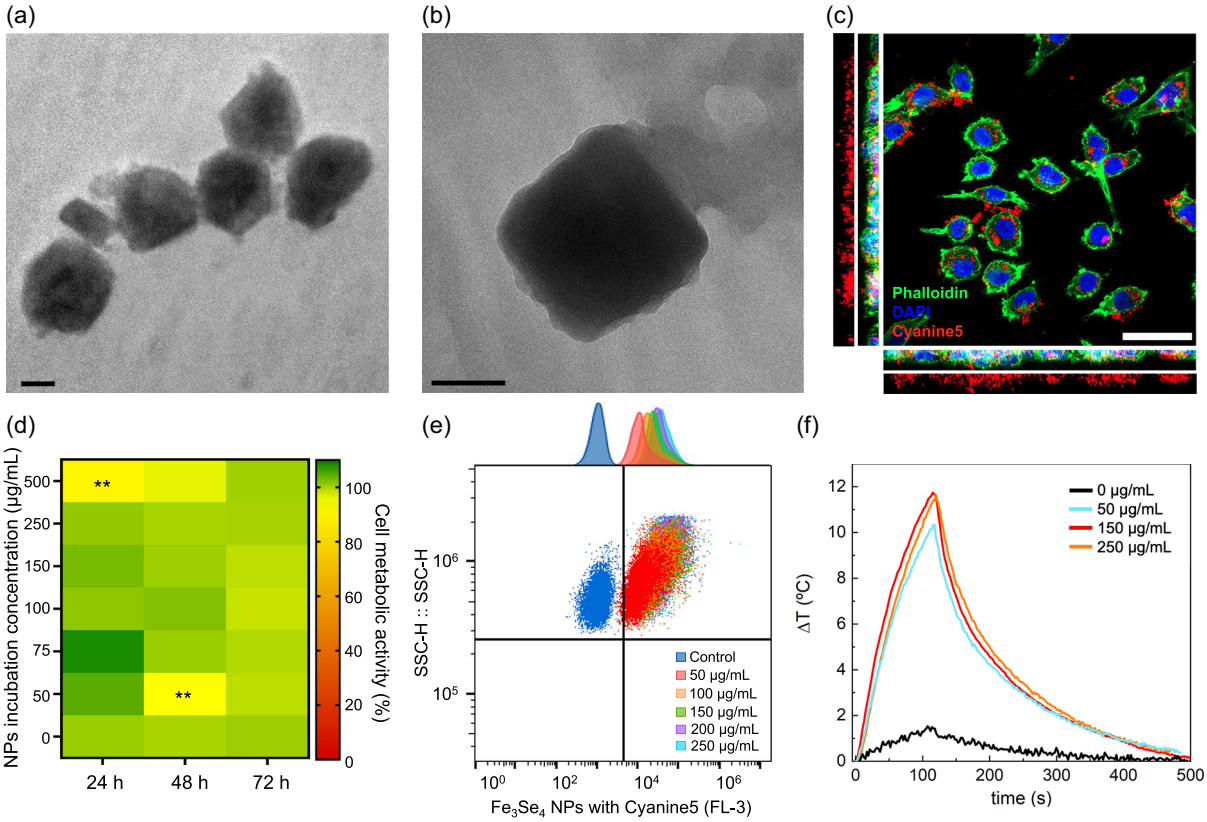


**Figure 2.** a,b) Transmission electron microscopy images of $Fe_3Se_4$ NPs (scale bar = 100 nm); c) confocal laser scanning micrograph of $Fe_3Se_4$ NPs interaction and internalization in L929 cells, incubation concentration of 100 μg $mL^{-1}$, with orthogonal projections for all channels and also only for Cyanine5. DAPI (blue channel) indicates cell nuclei, Flash phalloidin green 488 (green channel) indicates actin, and Cyanine5 (red channel) indicates $Fe_3Se_4$ NPs (scale bar = 50 μm); d) heat map evaluating L929 cells metabolic activity up to 72 h after incubation with $Fe_3Se_4$ NPs. Data are represented as mean ± s.d. ($n = 5$), $^{**}p < 0.05$; e) flow cytometry analysis of the cellular uptake of $Fe_3Se_4$ NPs with Cyanine5 (incubation concentration from 50 to 250 μg $mL^{-1}$); and f) heating curves of the 3D cellular assemblies with $Fe_3Se_4$ NPs at different incubation concentrations, obtained with a 808 nm laser at power density of 0.9 W $cm^{-2}$ for 120 s.

which revealed that the NPs were associated with the cells, whether being internalized or at the membrane (Figure 2c, S6, and S7, Supporting Information). From these images, it is not possible to access if there is a size-dependent internalization. The confocal imaging results were further validated by flow cytometry, which showed a fluorescence signal that increased with higher NPs doses (Figure 2e and S8, Supporting Information).

The $Fe_3Se_4$ NPs have a strong absorption in a broad range from UV to visible light, to NIR, including the two relevant optical windows of tissues (Figure 2f and S9, Supporting Information). The heating ability of $Fe_3Se_4$ NPs at 808 nm in fabricated 3D cellular assemblies was accessed in the NPs incubation concentration range of 0–250 μg $mL^{-1}$ with a laser at power density of 0.9 W $cm^{-2}$ for 120 s. This NIR dose resulted in a

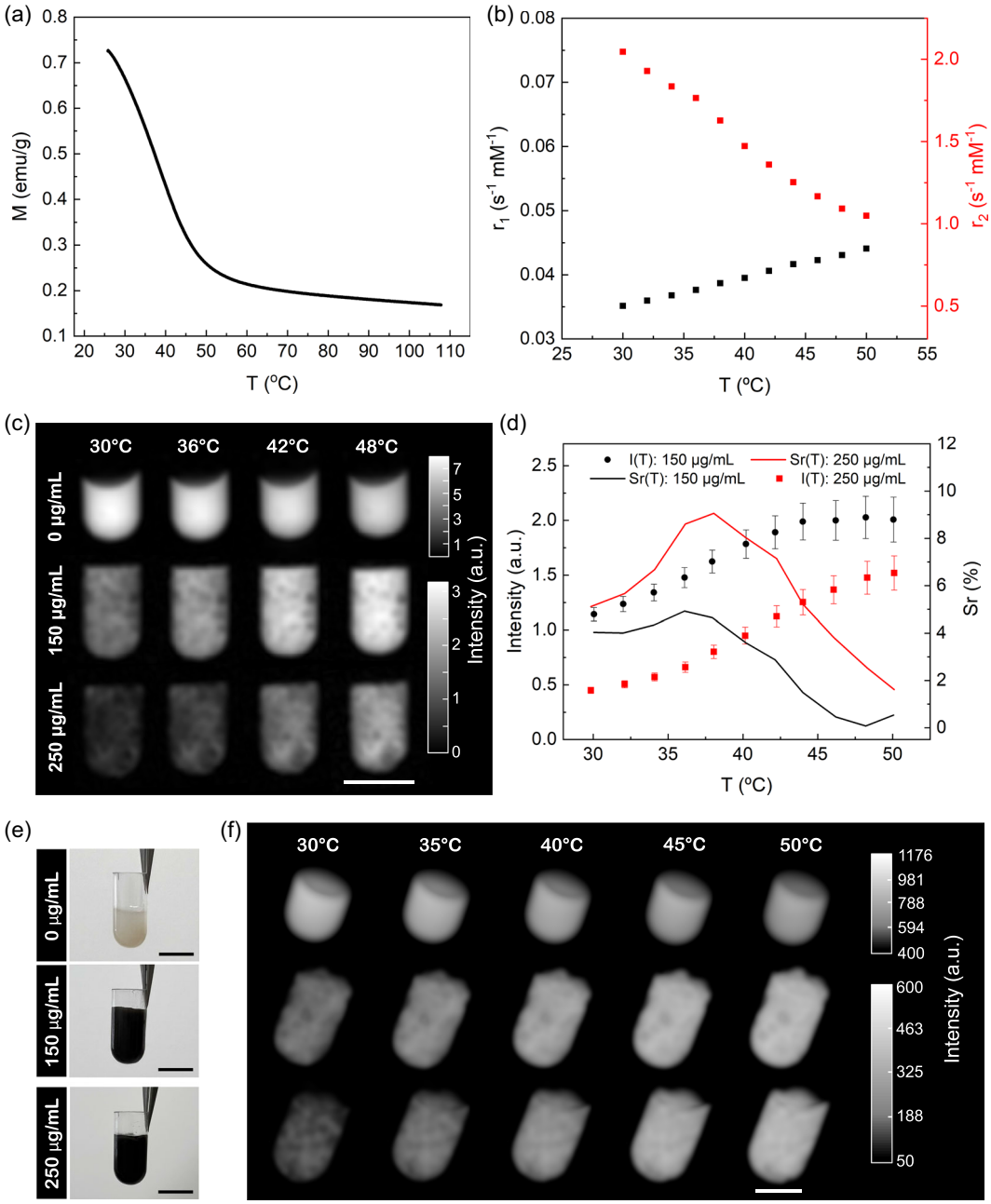


**Figure 3.** a) Dependence of the magnetization of $Fe_3Se_4$ NPs with temperature at 0.5 T; b) variation of $r_1$ and $r_2$ with temperature of the 3D cellular assemblies with $Fe_3Se_4$ NPs; c) 2D gradient echo (GE) images of 3D cellular assemblies with and without NPs over controlled temperature (scale bar = 5 mm); d) variation of the intensity of the 2D MRI GE images of the samples with 150 and 250 μg $mL^{-1}$ incubation concentration of NPs over temperature and respective relative variation; e) images of the prepared 3D cellular assemblies with and without NPs (scale bar = 5 mm), and f) 3D GE images of 3D cellular assemblies with and without NPs over controlled temperature (scale bar =3 mm). The large variation of magnetization shown in (a) leads to a large variation of $r_1$ and $r_2$ (b), which in turn results in the large variation of intensity of the MRI signal shown in (c,d,f).

temperature increase between 10 and 12 °C, depending on the NPs incubation concentration. The maximum specific absorption rate (SAR) value estimated from the initial slope of the time-temperature curves was 260 W $g^{-1}$ for the sample with a NPs incubation concentration of 50 μg $mL^{-1}$ (Figure S10, Supporting Information). These results show the ability of $Fe_3Se_4$ NPs as photothermal agents.

At the core of the temperature sensitivity observed in MRI is an order–disorder magnetic phase transition observed in $Fe_3Se_4$ NPs at around 45 °C (**Figure 3**a and S11, Supporting Information), making these NPs suitable for temperature sensing in the context of bioapplications. This magnetic phase transition is virtually immune to surrounding parameters other than temperature, such as viscosity, pH, and saline concentration, making magnetic NPs with such a phase transition particularly suitable for temperature sensing. The magnetic phase transition is associated with a strong decrease of the net magnetic moment of each NP. This net magnetic moment is the vector sum of the magnetic moments of all $Fe^{2+}$ and $Fe^{3+}$ ions of the NP, being well ordered at low temperatures. When approaching the transition temperature, their fluctuation increases and their intra-NP order is lost, resulting in the above-mentioned decrease of the net magnetic moment of each NP. The net magnetic moment is responsible for creating a dipolar magnetic field that perturbs the relaxation of the spins of the surrounding protons: the higher this perturbation is, the more

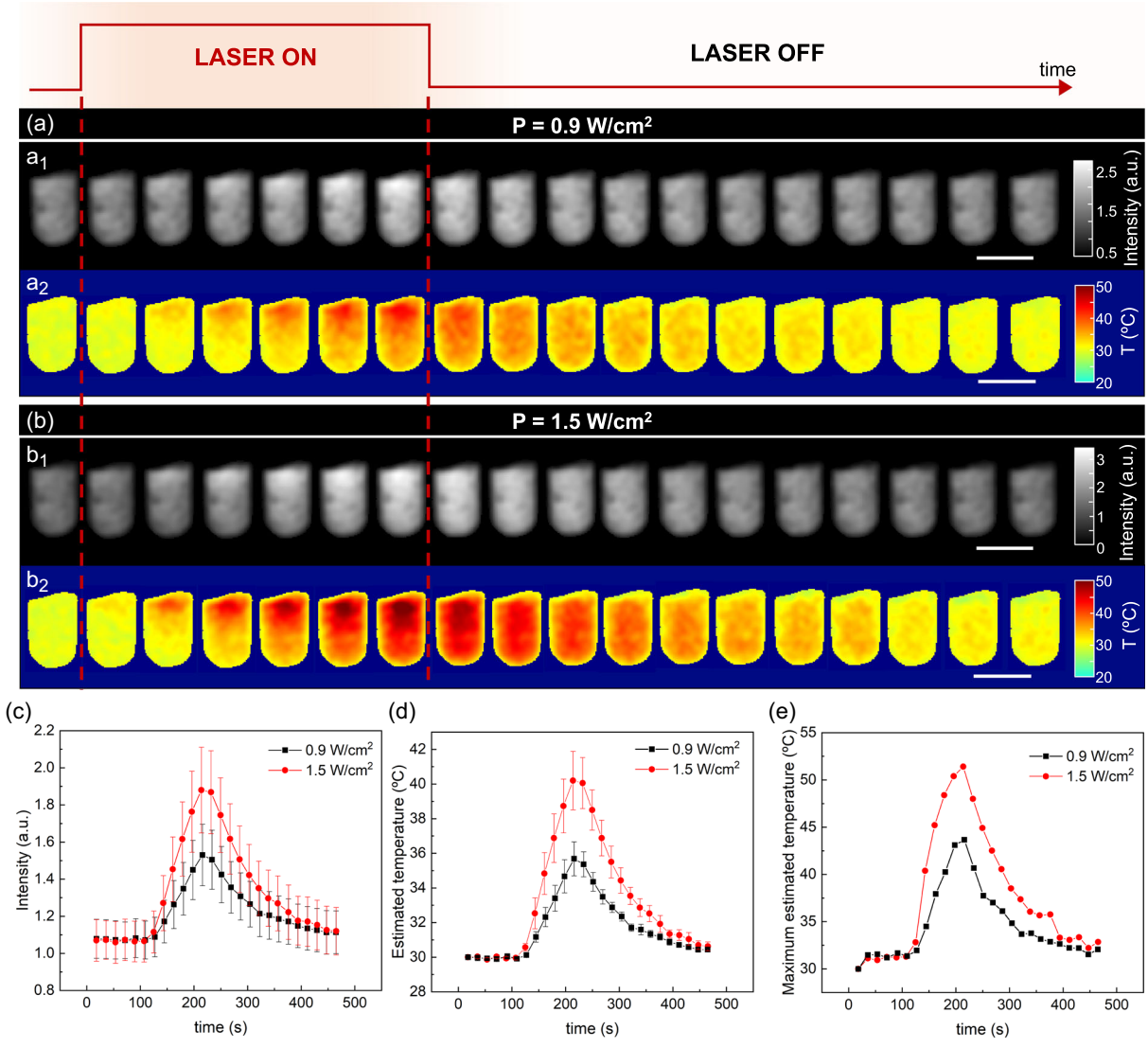


**Figure 4.** a) 2D $T_2^*$-weighted images of a 2D slice of the sample ($a_1$ and $b_1$) and associated temperature maps ($a_2$ and $b_2$) determined through the obtained 2D calibrations with the cellular assembly (150 μg $mL^{-1}$ incubation concentration of $Fe_3Se_4$ NPs) before, under, and after NIR irradiation for 120 s at 0.9 W $cm^{-2}$ and b) 1.5 W $cm^{-2}$ (scale bar = 5 mm); c) variation of the average intensity of the MRI image at the ROI during the laser experiment; d) variation of the average estimated temperature and e) maximum estimated temperature from the images during the laser experiment. The error bars in (c,d) are a measure of the temperature heterogeneity across the ROI. Error bars associated with temperature uncertainty, obtained at thermal equilibrium, are shown in Figure S16 and S17, Supporting Information. Please see the Supporting Information videos with the temporal evolution of the MRI images and temperature maps.

"efficient" the contrast agent is expected to be, being this "efficiency" measured as a longitudinal and transverse relaxivity ($r_1$ and $r_2$, respectively). It is thus expected that the decrease of the net magnetic moment with temperature leads to a decrease of the relaxivity.

As temperature increases, $r_2$ has a large decrease, confirming the ability of the $Fe_3Se_4$ NPs to generate a temperature-dependent contrast, which is the base of MRI thermometry based on contrast agents (Figure 3b, S12, and S13, Supporting Information). The existence of a large variation of $r_2$ with temperature opens the possibility to obtain MRI images with temperature-dependent intensity when exploring $T_2$-, or $T_2^*$-weighted sequences. In fact, 2D $T_2^*$-weighted gradient echo (GE) images of a 2D slice of the sample obtained with temperature (where the temperature of the samples was increased in a controlled way to a known value) and with similar echo times in 3D cellular assemblies loaded with $Fe_3Se_4$ NPs show a temperature-dependent increase of intensity up to 4.9 and 9.1% $°C^{-1}$, for the samples with NPs incubation concentration of 150 and 250 $\mu g\,mL^{-1}$, respectively, while the control sample

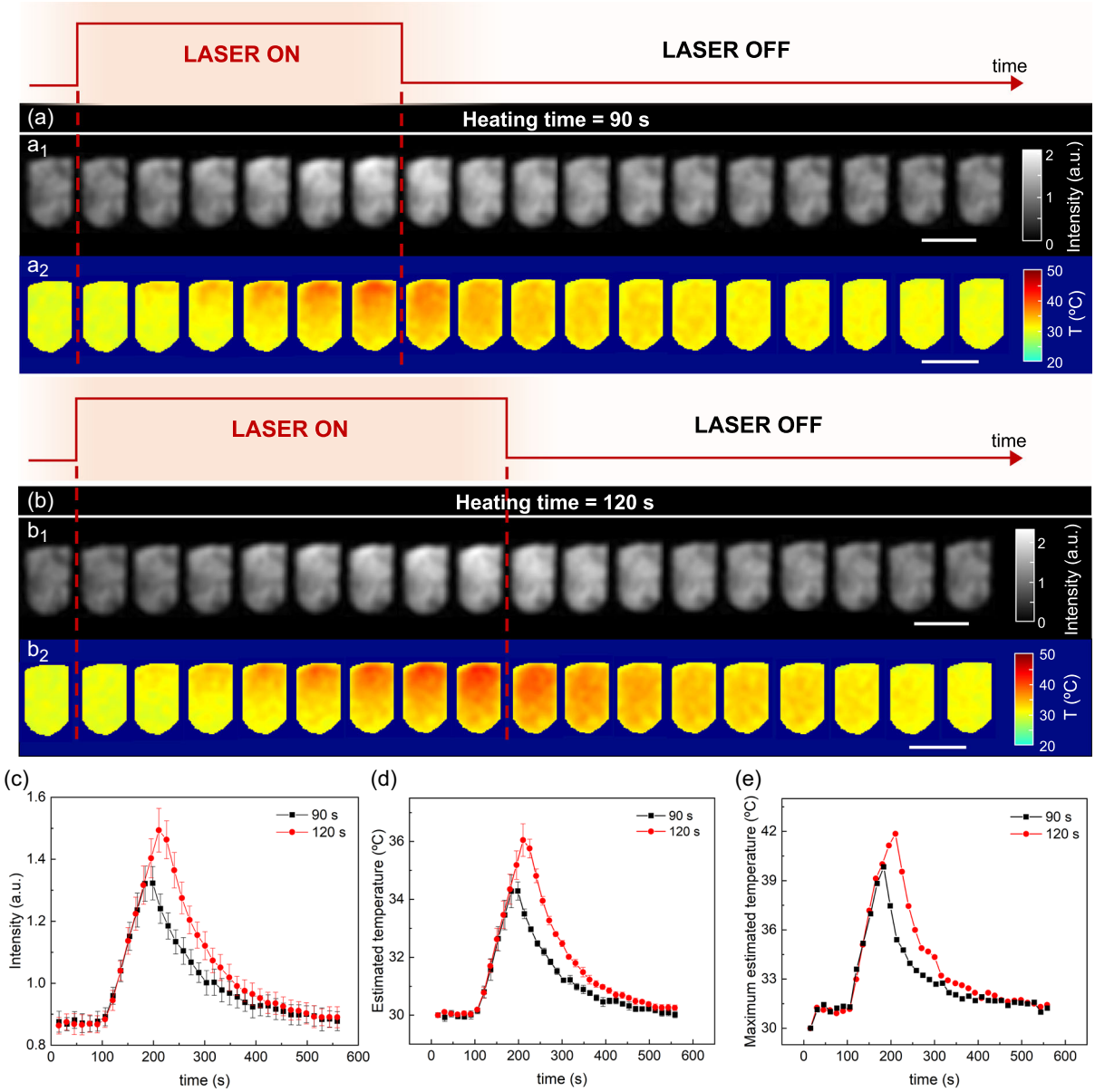


**Figure 5.** a) 2D $T_2^*$-weighted images of a 2D slice of the sample ($a_1$ and $b_1$) and associated temperature maps ($a_2$ and $b_2$) determined through the obtained calibrations with the 3D cellular assembly (250 $\mu g\,mL^{-1}$ incubation concentration of $Fe_3Se_4$ NPs) before, under, and after NIR irradiation at 0.9 W $cm^{-2}$ for 90 s and b) 120 s (scale bar = 5 mm); c) variation of the MRI image at the ROI during the laser experiment; d) variation of the average estimated temperature and e) maximum estimated temperature from the images during the laser experiment. The error bars in (c,d) are a measure of the temperature heterogeneity across the ROI. Error bars associated with temperature uncertainty, obtained at thermal equilibrium, are shown in Figure S16 and S17, Supporting Information. Please see the Supporting Information Videos with the temporal evolution of the MR images and temperature maps.

without NPs had an average intensity decrease up to 1.5% °C$^{-1}$ (Figure 3c,d, and S15, Supporting Information). The ability of the $Fe_3Se_4$ NPs to generate a temperature-dependent contrast can be also measured by the ratio between the control sample and samples with NPs (Figure S15b, Supporting Information). For the most concentrated sample, this ratio decreases more than 3 times across the 30–50 °C temperature range.

The validation of the NPs low cytotoxicity and their incorporation in 3D cellular assemblies, together with the validation of a good photothermal efficiency and high-temperature sensitivity in a single NP system, opens the way for a real-time 2D and 3D temperature mapping in the 3D cellular assemblies during NIR irradiation (**Figure 4** and **5**). Before the laser is turned on, the average MRI intensity is fairly constant across the 3D

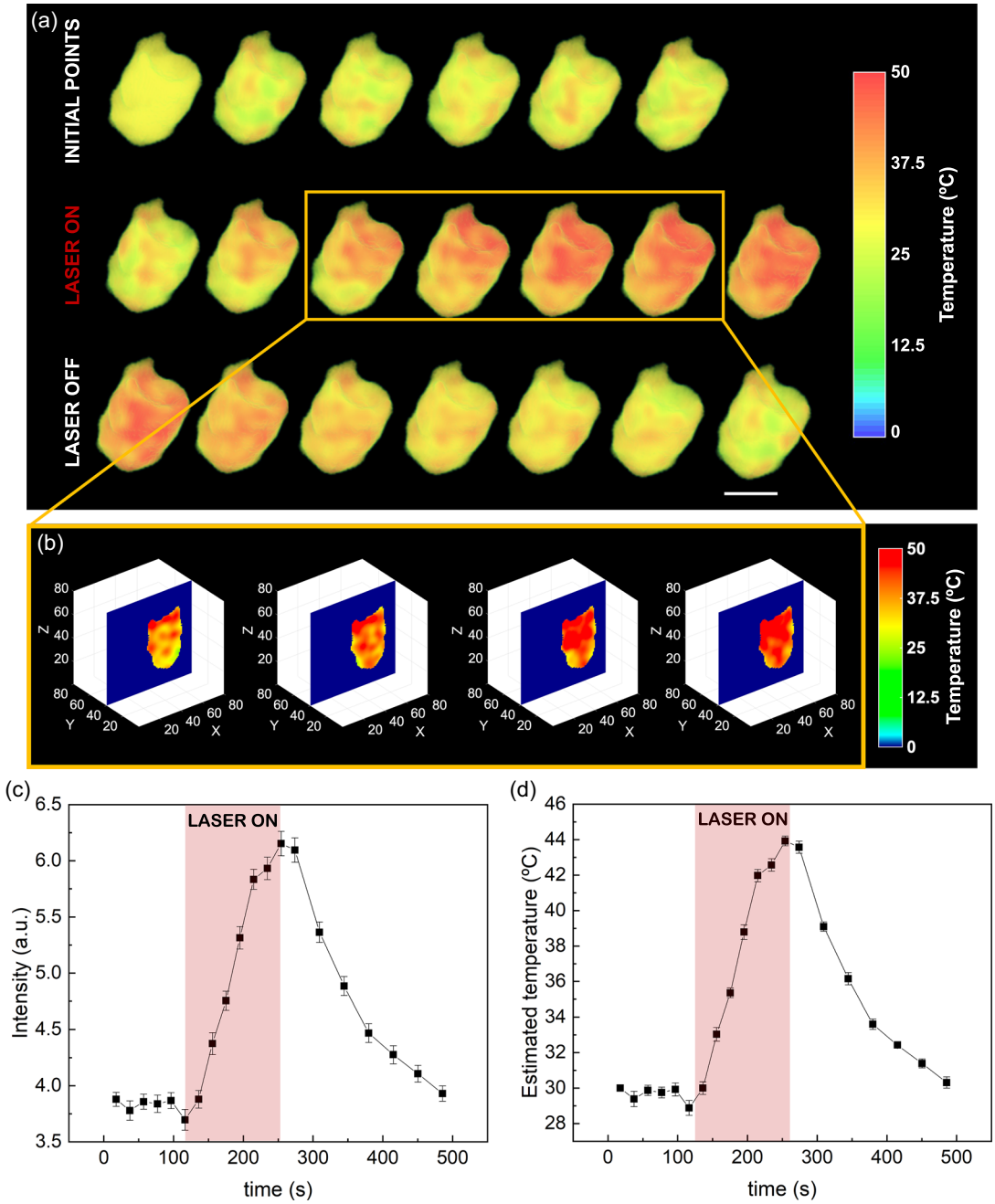


**Figure 6.** a) 3D temperature maps obtained with a cell sample (250 µg mL$^{-1}$ incubation concentration of $Fe_3Se_4$ NPs) before, under, and after NIR irradiation for 120 s at 1.5 W cm$^{-2}$ (scale bar = 3 mm); b) 2D projection of a slice of the 3D temperature map in the *xz* plane during laser irradiation; c) variation of the average intensity of the ROI during the laser experiment; and d) variation of the average temperature estimated from the intensity images during the laser experiment. The associated MRI intensity images are shown in Figure S22, Supporting Information. Please see the Supporting Information Videos with the temporal evolution of the MR images and temperature maps.

cellular assembly and so is the temperature (Figure 4c,d, and 5c, d). Some heterogeneities are noticeable, likely due to the nonuniform density of cells in the assembly (random cell assembly) or due to the distribution of NPs in the sample (Figure 4a,b and 5a, b) (please see also Supporting Information Videos). As the laser is turned on, the average intensity increases steadily. A few seconds after the laser is turned on, an increase in temperature is readily detected on the top of the 3D cellular assemblies (the region of incidence), expanding to regions farther away as time increases. After the laser is turned off, the temperature decreases back to a value close to the initial value, showing the reversibility of the system and the reversibility of the temperature sensing method. In other words, whatever changes occur in the 3D cellular assemblies that can in principle contribute to a change in MRI intensity, like dehydration, changes in the density of protons or their environment, do not have a relevant contribution to the image when compared to the dominant contribution of the temperature-dependent relaxivity of the $Fe_3Se_4$ NPs.

When the average across the volume is extracted, an average temperature increase of 5.7 and 10.2 °C was measured in the sample with 150 μg mL$^{-1}$ incubation concentration of NPs in the experiments with laser power of 0.9 and 1.5 W cm$^{-2}$, respectively, for 120 s. For the sample with 250 μg mL$^{-1}$ incubation concentration of NPs, an average temperature increase of 4.3 and 6.0 °C was measured for the laser duration of 90 and 120 s, respectively, at 0.9 W cm$^{-2}$. However, this average temperature variation hides transient temperature differences within the sample, as observed by the graphic of the maximum estimated temperature measured in the sample (Figure 4e and 5e). We hypothesize that since the top of the sample is constantly being irradiated during the heating time, this method detects differences that would be overlooked in a simple measurement with a thermocouple or equivalent. While the average reveals the abrupt increase and decrease of temperature that is often observed and expected for conduction mechanisms, the heat and the temperature maps provided by the $Fe_3Se_4$ NPs reveal the details of the temporal and space evolution of temperature and the details of its heterogeneity. These images were acquired with a pixel lateral size of ≈100 μm and temporal resolution of 18 and 15 s for the sample incubated with 150 and 250 μg mL$^{-1}$ of $Fe_3Se_4$ NPs, respectively. These 2D temperature maps were obtained with an average accuracy of 0.7 ± 0.5 and 1.0 ± 0.7 °C for the sample with 150 and 250 μg mL$^{-1}$ of NPs, respectively, in the temperature range between 30 and 50 °C (Figure S16 and S17, Supporting Information). The obtained accuracy is similar to the values reported in other studies, which is around 1 °C.[6,8,10,11]

While 2D temperature monitoring of thermal therapies using magnetic NPs for MRI thermometry represents a significant advancement in the field, it is essential to ensure complete monitoring of the entire irradiated volume for accurate and effective treatment outcomes. Considering that tissues are 3D in nature, developing tools for monitoring temperature at a higher scale than two-dimensions is highly needed not only to follow therapies at a clinical context, but also from a tissue engineering design perspective, especially considering the recent advances in bioengineering cell-dense 3D tissues at a laboratory scale.[16]

To achieve 3D temperature monitoring that better controls the depth and spread of heat on the entire volume of the sample, a fast 3D GE sequence was used. This sequence allowed to obtain 3D images within 20 s and with a voxel lateral size of 125 μm for the sample incubated with 250 μg mL$^{-1}$ of $Fe_3Se_4$ NPs. From the MRI images, 3D temperature maps were obtained with an average temperature accuracy of 0.9 ± 0.5 °C (**Figure 6**, S21, and S22, Supporting Information). The images show a heterogeneous increase of temperature from top to bottom, since the laser is irradiating from the top of the sample (please see also Supporting Information Videos). While the increase and decrease profile of the average temperature shows the typical exponential profiles found in single-point temperature measurements, and a maximum *average* increase of temperature of 14.3 °C (Figure 6d), the real-time 3D images show a much better insight on the dose (temperature and time) that each part of the 3D cellular assembly is experiencing, revealing transient temperature differences across the sample up to almost ≈15 °C. In the context of photothermal therapies, this heterogeneity may result in a heterogeneity of effects in cells and, ultimately, lead to different cell fates.

## 3. Conclusion

In summary, the $Fe_3Se_4$ NPs here reported open the way for simultaneous and efficient local NIR cellular heating and 3D temperature mapping in space and time, due to their key properties: absorption in the NIR, a magnetic phase transition around 45 °C, and a very high magnetic anisotropy that makes this transition sharp even when the material is in the form of NPs and not in its bulk form. This enables 3D temperature monitoring and control during laser photothermal therapy: control of the maximum achieved temperature, control of the doses, and control of the depth and extension of the therapy, with an accuracy ≤1 °C, overcoming all the limitations in conventional 2D measurements. This simultaneous heating ability and 3D temperature monitoring widen the range of real situations where the benefit of the temperature-controlled thermal therapy overcomes its associated risks, opening to way to real applications of thermometric photothermal agents. In particular, this 3D temperature measurement technique is expected to be translatable to different cell types and is expected to be well-suited for in vivo therapies based on local perfusion or local insertion of the photothermal or photodynamic agents, where the concentration of the agents is of the same order of that used here.[17]

The combination of thermometric NPs with low-field, lower-cost, and portable MRI scanners opens the way to 3D real-time temperature mapping in a wider range of contexts, particularly in opaque systems and in systems where in-depth temperature information is mandatory.

## 4. Experimental Section

*Materials*: Iron(III) 2,4-pentanedionate, selenium powder 99+%, 1-Octadecene tech. 90%, Dopamine hydrochloride, 99%, and tryethylamine, 99% were purchased from Alfa Aesar GmbH (Kandel, Germany). Ethanol absolute ≥99.8% AnalaR NORMAPUR ACS, Reag. and Dichloromethane ≥99.5% were purchased from VWR International (Radnor, USA). n-Tetradecylphosphonic acid was purchased from PlasmaChem GmbH (Berlin, Germany). 1-Dodecanethiol and N,N-Dimethylformamide were purchased from Merck KGaA (Darmstadt,

Germany). Fetal bovine serum (FBS, E.U. approved, South America origin), Dulbecco's Modified Eagle Medium-Low Glucose (DMEM-LG), Antibiotic-Antimycotic (ATB, Gibco - 10 000 units $mL^{-1}$ of penicillin, 10 000 mg $mL^{-1}$ of streptomycin, and 25 mg $mL^{-1}$ of Gibco Amphotericin B), TrypLE Express, phosphate buffered saline without $Ca^{2+}$ and $Mg^{2+}$ (dPBS, pH = 7.4), DAPI (4',6-diamidino-2-phenylindole, dihydrochloride), and AlamarBlue cell viability reagent were purchased from ThermoFisher Scientific (Alfagene, Carcavelos, Portugal). The mouse fibroblast L929 cell line (ref 85011425) was purchased from Sigma-Aldrich. Sulfo-Cyanine5 NHS ester was purchased from Lumiprobe GmbH (Hannover, Germany). Flash Phalloidin Green 488 was purchased from Biolegend (USA). Triton X-100 was purchased from Sigma-Aldrich.

*Synthesis of $Fe_3Se_4$ NPs*: $Fe_3Se_4$ NPs were prepared using Iron(III) 2,4-pentanedionate (Fe(acac) (III)) and Selenium-Octadecene (Se-ODE) as iron and selenium precursors, respectively. The synthesis of Se-ODE was adapted from the previous work of Bullen et al.[18] To prepare $Fe_3Se_4$ NPs, 1-Dodecanethiol (DDT) and n-Tetradecylphosphonic acid (TDPA) were used as organic coordination ligands that control the formation and growth of the NPs.

*Synthesis of Se-ODE*: In a round bottom flask, 283 mg of selenium powder was dissolved in 154 g of 1-Octadecene (ODE). The mixture was purged under vacuum at 120 °C. After 1 h, the mixture was then placed under a nitrogen atmosphere and the temperature was increased to 215 °C. After 10 min the reaction was cooled to room temperature (RT) and reserved in a flask for further usage.

*Synthesis of $Fe_3Se_4$ NPs*: In a round bottom flask, 58.5 mg of Iron(III) 2,4-pentanedionate, 10.2809 g of Se-ODE, 15.3 mg of DDT, and 23.7 mg of TDPA were mixed and purged in vacuum at 70 °C. After 1 h, the mixture was placed under a nitrogen atmosphere and heated up to 250 °C for 30 min with a heating rate of 5 °C $min^{-1}$. The reaction was then cooled to RT and the NPs were washed with Dichloromethane and collected through centrifugation (2000 rpm, 20 min, RT).

*$Fe_3Se_4$ NPs Phase Transfer and Functionalization*: In a Schlenk tube, 10 mg of $Fe_3Se_4$ NPs was dispersed in 5 mL of N,N-Dimethylformamide using an ultrasonic bath. Then, 50 mg of dopamine hydrochloride was added and the mixture was then stirred at 50 °C under $N_2$ for 3 h. After that time, 5 µL of tryethylamine and 5 mL of N,N-Dimethylformamide were added and the temperature was cooled to 25 °C. After 20 h, the obtained mixture was collected and centrifuged to remove all the N,N-Dimethylformamide and then dispersed in water. A similar procedure was made replacing dopamine hydrochloride by caffeine acid. The validation of phase transfer with two molecules with two different functional groups widens the possible routes for subsequent functionalization.

For microscopy analysis, an additional step was performed by adding sulfo-Cyanine5 NHS ester to the NPs surface. The $Fe_3Se_4$ NPs were resuspended in water at a final concentration of 10 mg $mL^{-1}$, and 100 µL of this solution was added to 900 µL of a sodium bicarbonate buffer (0.1 M, pH = 8.3). Then, 10 µL of a stock solution of sulfo-Cyanine5 NHS ester in dimethyl sulfoxide (DMSO), with a concentration of 10 mg $mL^{-1}$, was added to the mixture and left stirring at RT for 2 h. The NPs were washed with distilled water and centrifuged 5× (2000 rpm, 10 min, RT) to guarantee that the excess dye was removed.

*$Fe_3Se_4$ NPs Structural Characterization*: X-ray diffraction (XRD) measurements were performed at RT with a PANalytical Empyrean powder diffractometer using monochromated $CuK_\alpha$ radiation ($\lambda = 1.541$ Å) in the $10 - 100°(2\theta)$ range at 0.02° resolution, and 4000 acquisition points per step. The incident beam optics included a Soller slit of 0.04 rad, a 10 mm fixed mask, a divergence fixed slit of 1/4, and an antiscatter slit of 1/8. The diffracted beam optics included a Soller slit of 0.04 rad and antiscatter slit of 7.5 mm. The analysis of the diffraction patterns was performed by Rietveld refinement using the FullProf Suite. The size effects were treated with the integral breadth method using the Voigt model for both the instrumental and intrinsic diffraction peak shape considering a Thompson–Cox–Hastings pseudo-Voigt convoluted with Axial divergence asymmetry function to describe the peak shape. The contribution of the instrument to the peaks broadening was determined by the refinement of the XRD pattern of a $LaB_6$ standard sample (NIST ref. 660a).

*$Fe_3Se_4$ NPs Magnetic Characterization*: The magnetic response of $Fe_3Se_4$ NPs was investigated using a vibrating-sample magnetometer (VSM, LakeShore 8600). For these studies, powder samples of $Fe_3Se_4$ NPs were prepared. The hysteresis curves of the NPs were obtained at RT between +20 and −20 kOe. The temperature dependence of the NPs magnetization was studied in the temperature range of 25–70 °C at a low-field value (50 Oe) and at a field close to that of the MRI (5 kOe).

*2D In Vitro Cell Culture*: A mouse fibroblast cell line (L929) was maintained in 175 $cm^2$ T-flasks with DMEM-LG supplemented with 10% v/v FBS and 1% v/v ATB in a humidified and controlled atmosphere (5% $CO_2$), at 37 °C. Whenever cells reached 70–80% confluency, they were harvested by TrypLE Express, ideal for dissociating attachment-dependent cell lines.

*$Fe_3Se_4$ NPs Cytotoxicity Evaluation*: The cytotoxicity of $Fe_3Se_4$ NPs was accessed by using the Alamar Blue assay. Briefly, L929 cells were seeded in adherent 96-well plates at a density of $20 \times 10^3$ cells per well. After 24 h, the medium was replaced by a mixture of culture medium (DMEM-LG with FBS and ATB) and $Fe_3Se_4$ NPs at final concentrations of 50, 75, 100, 150, 250, and 500 µg $mL^{-1}$, and incubated for 24 h. Afterward, the medium was replaced with fresh medium. After the time points, the medium of each well was replaced with a mixture of Alamar Blue (10 µL) and culture medium (100 µL), and incubated for 4 h in a incubator. After incubation, the resorufin fluorescence was quantified by fluorescence measurements ($\lambda_{ex} = 500$ nm, $\lambda_{em} = 600$ nm), in a Synergy HTX multimode microplate reader by using a 96-well black-clear bottom plate.

*$Fe_3Se_4$ NPs Cellular Uptake*: The interaction and internalization of the NPs in cells were evaluated by confocal laser scanning microscopy, for a qualitative analysis, and by flow cytometry, for a quantitative analysis. For confocal-based bioimaging, L929 cells were seeded in adherent ibidi µ-slide 8 well plates at a density of $25 \times 10^3$ cells per well. After 24 h, a mixture of $Fe_3Se_4$ NPs with Cyanine5 and culture medium (DMEM-LG with FBS and ATB) was added to each well at final concentrations of 50, and 100 µg $mL^{-1}$ and incubated for 24 h. Afterward, cells were washed 3× with dPBS, fixed with paraformaldehyde (PFA) (4% v/v in PBS, 30 min, RT), and permeabilized with a solution of Triton X-100 (0.5% v/v in PBS, 15 min, RT). After washing the cells with dPBS, cells were stained with Flash Phalloidin Green 488 (1:100 in PBS, 45 min, RT) and then with DAPI (1:250 in PBS, 15 min, RT). Cells were observed in a Zeiss LSM 900 confocal laser scanning microscope equipped with a GaSP detector (Carl Zeiss Microscopy, Germany). Images were analyzed in the ImarisViewer 10.1 software.

For flow cytometry analysis, L929 cells were seeded in 12-well plates at a density of $250 \times 10^3$ cells per well. After 24 h, a mixture of $Fe_3Se_4$ NPs with cyanine5 and culture medium was added to each well at final concentrations of 50, 100, 150, 200, and 250 µg $mL^{-1}$ and incubated for 24 h (3 wells for each condition). After that time, each well was washed 3× with dPBS, harvested with TrypLE Express, and centrifuged (300G, 5 min, RT). The cells were resuspended in dPBS and, after being filtered by a 40 µm cell strainer, were analyzed in a BD Accuri C6 plus flow cytometer equipped with a 488 nm laser. For each sample, $10 \times 10^3$ events were acquired in the selected region of interest. As for control, sample of $Fe_3Se_4$ NPs without cyanine5 were also prepared in the same conditions. Images were analyzed in the FlowJo software (Ashland,Oregon, USA).

*Fabrication of 3D Cellular Assemblies with $Fe_3Se_4$ NPs*: For laser and MRI studies, L929 3D cellular assemblies with $Fe_3Se_4$ NPs were prepared. Briefly, for each condition, L929 cells were seeded in three 6-well plates at a density of $500 \times 10^3$ cells per well. After 48 h, a mixture of $Fe_3Se_4$ NPs and culture medium (DMEM-LG with FBS and ATB) at final incubation concentrations of 50, 150, and 250 µg $mL^{-1}$ was added at final volume of 1 mL and incubated for 24 h. After that time, cells were washed 3× with dPBS and then harvested with TrypLE Express and the cells from the three plates (of the same conditions) were added to an eppendorf and centrifuged (300G, 5 min, RT). Additionally, a control sample (3D cellular assembly without NPs) in the same conditions was also prepared. The resulting samples were then fixed with PFA 4% and washed 2× with dPBS. For laser and MRI studies, the dPBS in excess was removed. The samples were placed inside capsules with a diameter of 5 mm, and stored in dPBS at 4 °C.

**Table 1.** $T_2^*$-weighted images sequence parameters used to compare the contrast over concentration and temperature.

| Incubation concentration [μg mL$^{-1}$] | $T_E$ [ms] | $T_R$ [ms] | Acquisition time [s] | Number of pixels | Image size [mm] | Pixel/voxel lateral size [mm] |
|---|---|---|---|---|---|---|
| 2D images | | | | | | |
| 0 | 2 | 1500 | 106 | 128 × 128 | 10 × 10 | 0.078 |
| 50 | 5 | 500 | 35 | | | |
| 150 | 5 | 300 | 21 | | | |
| 250 | 5 | 250 | 17 | | | |
| 3D images | | | | | | |
| 0 | 2 | 1500 | 778 | 32 × 32 × 32 | 10 × 10 × 10 | 0.313 |
| 150 | 3 | 300 | 616 | 64 × 64 × 64 | 10 × 10 × 10 | 0.156 |
| 250 | 3 | 250 | 513 | | | |

The total mass of each sample and the respective amount of $Fe_3Se_4$ NPs and iron in each one, as well as the iron concentration, are represented in **Table 1** in Supporting Information. The incubation concentration represents the concentration of the sample (with organic and inorganic components) dispersed in cell culture medium that was incubated in each well of the plate for each condition. The total sample mass represents the total mass of the sample for each condition (i.e., adding the mass that was incubated in 3 plates of 6 wells for each condition). Afterward, to obtain only the mass of the inorganic component of the sample (i.e., only $Fe_3Se_4$ NPs) that was internalized or associated with the cells, the total mass was multiplied to a factor of 15 %. This factor was estimated by dividing the obtained saturation magnetization with the expected value (around 4 emu/g$Fe_3Se_4$, estimated with a sample of $Fe_3Se_4$ NPs with a known mass value), at RT. The Fe mass of the sample was then estimated. Finally, considering the volume of the final sample of 80 μL, the Fe concentration of the final samples was estimated. This method for Fe estimation grants consistency across different samples, since magnetic measurements are sensitive to about $10^{-6}$ emu, which corresponds to 0.25 μg of $Fe_3Se_4$. Any systematic error associated with the 4 emu/g$Fe_3Se_4$ value, would change the calibration factor between MRI intensity, mass, and temperature, but would not impact temperature uncertainty or accuracy.

*$Fe_3Se_4$ NPs Photothermal Effect Evaluation*: To understand the effectiveness of $Fe_3Se_4$ NPs in converting light into heat, 3D cellular assemblies with different incubation concentrations of NPs were irradiated with a 808 nm laser (MDL-III-808-1.5W, Photontec, Berlin) for 120 s at 0.9 W cm$^{-2}$. The initial temperature of the experiments was around 30 °C. The SAR was estimated by the equation

$$\mathrm{SAR} = \frac{c * m_s}{m_{NPs}} \frac{dT}{dt} \quad (1)$$

where c is the specific heat of the sample (we considered the specific heat of mice tissue, $c = 3.66\,\mathrm{J g^{-1}\,°C^{-1}}$ (lean mice with 8% fat)[19]), $m_s$ is the mass of the sample considering the final volume of 80 μL and fibroblast density of 1.03 g mL$^{-1}$,[20] $m_{NPs}$ is the mass of the $Fe_3Se_4$ NPs in each sample (only including the inorganic component), and $dT/dt$ is the initial slope of the heating curve (considering the first 10 points).[21]

*MRI Analysis*: 3D cellular assemblies were studied in a research MRI device (Pure Devices, 0.55 T), providing an homogeneity of 5 ppm in a field of view of 10 mm of diameter, maximum gradients of 1 T m$^{-1}$ ($x$,$y$) and 1.2 T m$^{-1}$ ($z$).

*Relaxation Times Measurement*: The relaxation times $T_1$ and $T_2$ were obtained as a function of temperature and concentration of NPs with an inversion recovery (IR) sequence and a Carr Purcell Meiboom Gill (CPMG) sequence, respectively. The relaxivities (longitudinal relaxivity ($r_1$) and transverse relaxivity ($r_2$) were obtained from the slopes of the curves of the relaxation rates ($1/T_1$ and $1/T_2$) with Fe concentration (mM) of the sample at several temperatures in the range of 30–50 °C.

*Images Acquisition*: To compare the contrast of the produced samples, 2D GE sequences with similar echo times ($T_E$) and long repetition times ($T_R$) were used to obtain 2D and 3D $T_2^*$-weighted contrast images as a function of temperature and concentration of NPs. The sequence parameters used for each sample are described in Table 1. The process of the formation of 3D MRI images is explained in Supporting Information.

For each image, a region of interest (ROI) was selected using the Image Segmenter tool in MATLAB. The mean intensity and standard deviation were determined with the values contained in the ROI. The relative variation was obtained through the derivative of the Neperian logarithm of the cubic polynomial approximation of the intensity as a function of temperature.

*Temperature Calibrations*: The previously acquired images had similar $T_E$, which facilitated a clearer comparison of the effects of NP concentration and temperature. However, these parameters do not provide the optimal variation of intensity with temperature. To achieve a better variation, new parameters were studied. These parameters were chosen to provide a balance between acquisition time, space, and temperature resolutions, which are entangled and, to a certain extent, one can be increased at the expenses of the other(s).

To obtain temperature maps, it is first needed to obtain calibrations to correlate the intensity with temperature, which are dependent on the concentration of NPs in the sample. To correlate the intensity of the samples with temperature, a system to control the temperature of the samples was assembled. This system regulated the temperature inside the MRI through an air flow. The samples were placed inside a tube and the air flow with variable temperature circulated through it. Using an external controller, the desired temperature was specified which, through a resistor, regulated the temperature of the air flow in contact with the sample. The temperature of the sample was controlled by a fiber-optic thermometer that was placed at the exterior surface of the capsule with the sample.

The 2D temperature calibration curves were obtained by acquiring 2D $T_2^*$-weighted images at known temperature values in the range of 30–50 °C. A fast 3D GE sequence was used to obtain 3D images of the samples in a shorter period of time. The same procedure used to obtain the 2D calibrations was applied to obtain the 3D calibration. The sequence parameters that allowed the best compromise between image acquisition duration and image intensity variation are described in **Table 2**.

**Table 2.** $T_2^*$-weighted images sequence parameters used to obtain the temperature calibrations.

| Incubation concentration [μg mL$^{-1}$] | $T_E$ [ms] | $T_R$ [ms] | Acquisition time [s] | Number of pixels | Image size [mm] | Pixel/voxel lateral size [mm] |
|---|---|---|---|---|---|---|
| 2D images | | | | | | |
| 150 | 4 | 300 | 67 (3 averages) | 128 × 128 | 10 × 10 | 0.078 |
| 250 | 3 | 250 | 57 (3 averages) | | | |
| 3D images | | | | | | |
| 250 | 4 | 7 | 20 | 80 × 80 × 80 | 10 × 10 × 10 | 0.125 |

For each pixel/voxel of the ROI, it was performed a linear regression of first order of the intensity as a function of temperature (an example is reported in Figure S16, Supporting Information). Two calibration methods were applied: one that estimates temperature variation and other absolute temperature. In the first approach, the average value of the slopes obtained for each of the pixels/voxels was used and applied to obtain the temperature of the pixel/voxel of the ROI as such

$$T_i = T_{i-1} + \frac{I_i - I_{i-1}}{s_m} \quad (2)$$

where $s_m$ is the average value of all the slopes obtained from the linear regressions of each pixels/voxels of the ROI and I is the intensity of the pixel/voxel. In this case, temperature variations are measured since this calibration assumes that the initial temperature is the same in the entire sample which, in this case, was considered 30 °C (Figure S16 and S17, Supporting Information). In the second approach, absolute temperature was measured. For this, the average value of the slopes and intercepts of the linear regressions obtained for each pixels/voxels were used as such

$$T_i = I_i * s_m + b_m \quad (3)$$

where $b_m$ is the average value of all the intercepts obtained from the linear regressions of all the pixels/voxels of the ROI (Figure S18, Supporting Information). **Table 3** showcases the 2D/3D calibration parameters used.

Taking a one-point optical thermometer as a reference, the temperature accuracy was estimated by subtracting the real temperature value given by the thermometer and the temperature obtained with the calibration method. The temperature error was estimated from the 2D MRI images used for the calibrations by the propagation error method. From Equation (2), the temperature error is given by

$$\sigma_{Ti} = \frac{1}{s_m} * \sigma_{Ii} \quad (4)$$

where $\sigma_{Ti}$ is the temperature error and $\sigma_{Ii}$ is the standard deviation of the intensity obtained from the calibration images.

The factors that impact the uncertainty of this technique are 1) the homogeneity of the NPs concentration and the mass of $Fe_3Se_4$ (that contributes to changes in $R_1$ and $R_2$, since $R_n = c^* r_n$, being $c$ concentration), 2) the homogeneity of cell concentration (that contributes to the MRI signal via the concentration of $^1H$), 3) the homogeneity of the intercell media properties, in particular concentration and diffusivity of $^1H$, that contributes to MRI signal, and 4) the $B_0$ field heterogeneity, particularly in the GE sequences. As long as each voxel includes a representative sample of the distribution of the NPs, the size distribution does not impact temperature uncertainty. This is expected to hold, since the voxel lateral size is about 500–1000 times higher than the size of each NP. In addition, the possible existence of a size-dependent internalization within the cells would be a relevant factor impacting temperature accuracy and uncertainty if subcell space resolution measurements would be performed. We do not access the individual contribution of each factor but their combined effect in the temperature accuracy and uncertainty.

*Laser Irradiation*: The same samples used to obtain the calibration curves were irradiated with a 808 nm inside the MRI device at two different power densities: 0.9 and 1.5 W cm$^{-2}$, and for two different time windows: 90 and 120 s. While the sample was being irradiated, 2D and 3D MRI images were acquired. The parameters used for image acquisition are described in **Table 4**. Before the laser was turned on, 6 images were acquired at RT. The setup of the experiment is represented in Figure S1, Supporting Information. After, the respective calibration curves were applied to the images to obtain temperature maps.

Raw data acquisition was performed in MATLAB R2024 and 3D images were reconstructed using VolView software (version 3.4, Kitware Inc., US).

**Table 3.** Calibration parameters used to estimate the temperature.

| Incubation concentration [μg mL$^{-1}$] | $s_m$ | $b_m$ |
|---|---|---|
| 2D images | | |
| 150 | 0.0795 | −0.9648 |
| 250 | 0.1041 | −2.1564 |
| 3D images | | |
| 250 | 0.1633 | −1.4244 |

**Table 4.** $T_2^*$-weighted images sequence parameters used to obtain MRI images during irradiation.

| Incubation concentration [μg mL$^{-1}$] | $T_E$ [ms] | $T_R$ [ms] | Acquisition time [s] | Number of pixels | Image size [mm] | Pixel/voxel lateral size [mm] |
|---|---|---|---|---|---|---|
| 2D images | | | | | | |
| 150 | 4 | 300 | 18 | 96 × 96 | 10 × 10 | 0.104 |
| 250 | 3 | 250 | 15 | | | |
| 3D images | | | | | | |
| 250 | 4 | 7 | 20 | 80 × 80 × 80 | 10 × 10 × 10 | 0.125 |

## Supporting Information

Supporting Information is available from the Wiley Online Library or from the author.

## Acknowledgements

This work was developed within the scope of the project CICECO-Aveiro Institute of Materials, UIDB/50011/2020, UIDP/50011/2020, and LA/P/0006/2020, financed by national funds through the Portuguese Foundation for Science and Technology/MEC (PIDDAC). The authors acknowledge the financial support by the Portuguese Foundation for Science and Technology (FCT) through the doctoral grants (2022.10039.BD, J.F.S., SFRH/BD/143320/2019, R.A.P.) and through an assistant researcher contract (DOI: 10.54499/2022.02106.CEE- CIND/CP1720/CT0028, V.M.G.). Additionally, this work was supported by grants PTDC/NAN-MAT/3901/2020 (DOI: 10.54499/PTDC/NAN-MAT/3901/2020 supported by POCI, FEDER, and FCT/MCTES) and grant ERC-2019-CoG-865437 from the European Research Council (ERC) under the European Union's Horizon 2020 research and innovation program. The funding of project O2Cells—"Hybrid living bioengineered hierarchical constructs with self-oxygenating capability", (ref. 2022.04237.PTDC) is also acknowledged. M.M. and A.L. acknowledge the partial funding by the Istituto Nazionale di Fisica Nucleare (INFN) (project "Mather3D").

## Conflict of Interest

The authors declare no conflict of interest.

## Author Contributions

**Joana F. Soeiro**: conceptualization (equal); data curation (lead); investigation (lead); methodology (equal); writing—original draft (equal); writing—review & editing (equal). **Rute A. Pereira**: investigation (equal). **Rui Oliveira-Silva**: investigation (equal); methodology (equal). **Filipa L. Sousa**: conceptualization (equal); funding acquisition (supporting). **Vítor M. Gaspar**: conceptualization (equal); funding acquisition (equal); resources (equal); supervision (equal); writing—review & editing (equal).

**João F. Mano**: funding acquisition (equal); resources (equal); supervision (supporting). **Ángel Millán**: conceptualization (supporting); investigation (supporting); writing—review & editing (supporting). **Claudia Innocenti**: conceptualization (supporting); investigation (supporting). **Manuel Mariani**: conceptualization (supporting). **Alessandro Lascialfari**: conceptualization (supporting); methodology (supporting); resources (supporting); supervision (supporting); writing—review & editing (supporting). **Nuno J. O. Silva**: conceptualization (lead); data curation (supporting); funding acquisition (lead); investigation (supporting); methodology (equal); resources (lead); supervision (lead); writing—original draft (equal); writing—review & editing (equal).

## Data Availability Statement

The data that support the findings of this study are available from the corresponding author upon reasonable request.

## Keywords

3D temperature imaging, cellular hyperthermia, magnetic resonance imaging thermometry, simultaneous heat generation and temperature mapping

Received: December 12, 2024
Revised: March 31, 2025
Published online: May 23, 2025

[1] J. Zhou, B. Del Rosal, D. Jaque, S. Uchiyama, D. Jin, *Nat. Methods* **2020**, *17*, 967.
[2] M. Quintanilla, L. M. Liz-Marzán, *Nano Today* **2018**, *19*, 126.
[3] Y. Wu, F. Li, Y. Wu, H. Wang, L. Gu, J. Zhang, Y. Qi, L. Meng, N. Kong, Y. Chai, Q. Hu, Z. Xing, W. Ren, F. Li, X. Zhu, *Nat. Commun.* **2024**, *15*, 2341.
[4] V. Rieke, K. Butts Pauly, *J. Magn. Reson. Imaging* **2008**, *27*, 376.
[5] F. Settecase, M. S. Sussman, T. P. L. Roberts, *Contrast Media Mol. Imaging* **2007**, *2*, 50.
[6] J. H. Hankiewicz, Z. Celinski, K. F. Stupic, N. R. Anderson, R. E. Camley, *Nat. Commun.* **2016**, *7*, 12415.
[7] J. A. Nelson, L. H. Bennett, M. J. Wagner, *J. Am. Chem. Soc.* **2002**, *124*, 2979.
[8] N. A. Alghamdi, J. H. Hankiewicz, N. R. Anderson, K. F. Stupic, R. E. Camley, M. Przybylski, J. Żukrowski, Z. Celinski, *Phys. Rev. Appl.* **2018**, *9*, 054030.
[9] J. Stroud, Y. Hao, T. S. Read, J. H. Hankiewicz, P. Bilski, K. Klodowski, J. M. Brown, K. Rogers, J. Stoll, R. E. Camley, Z. Celinski, M. Przybylski, *Magn. Reson. Imaging* **2023**, *100*, 43.
[10] J. H. Hankiewicz, N. Alghamdi, N. M. Hammelev, N. R. Anderson, R. E. Camley, K. Stupic, M. Przybylski, J. Zukrowski, Z. J. Celinski, *AIP Adv.* **2017**, *7*, 056703.
[11] J. H. Hankiewicz, J. A. Stoll, J. Stroud, J. Davidson, K. L. Livesey, K. Tvrdy, A. Roshko, S. E. Russek, K. Stupic, P. Bilski, R. E. Camley, Z. J. Celinski, *J. Magn. Magn. Mater.* **2019**, *469*, 550.
[12] J.-. Jang, H. Nah, J.-H. Lee, S. H. Moon, M. G. Kim, J. Cheon, *Angew. Chem., Int. Ed.* **2009**, *48*, 1234.
[13] L. J. De Jongh, A. R. Miedema, *Adv. Phys.* **1974**, *23*, 1.
[14] R. Oliveira-Silva, R. A. Pereira, F. M. Silva, V. M. Gaspar, A. Ibarra, Á. Millán, F. L. Sousa, J. F. Mano, N. J. O. Silva, *Mater. Horiz.* **2019**, *6*, 524.
[15] Y. Liu, T. Chen, C. Wu, L. Qiu, R. Hu, J. Li, S. Cansiz, L. Zhang, C. Cui, G. Zhu, M. You, T. Zhang, W. Tan, *J. Am. Chem. Soc.* **2014**, *136*, 12552.
[16] P. Lavrador, B. S. Moura, J. Almeida-Pinto, V. M. Gaspar, J. F. Mano, *Nat. Mater.* **2025**, *24*, 143.
[17] K. Maier-Hauff, F. Ulrich, D. Nestler, H. Niehoff, P. Wust, B. Thiesen, H. Orawa, V. Budach, A. Jordan, *J. Neuro-Oncol.* **2011**, *103*, 317.
[18] C. Bullen, J. Van Embden, J. Jasieniak, J. E. Cosgriff, R. J. Mulder, E. Rizzardo, M. Gu, C. L. Raston, *Chem. Mater.* **2010**, *22*, 4135.
[19] P. Faber, L. Garby, *Acta Physiol. Scand.* **1995**, *153*, 185.
[20] C. Drobek, J. Meyer, R. Mau, A. Wolff, K. Peters, H. Seitz, *iScience* **2023**, *26*, 105796.
[21] C. Iacovita, I. Fizeşan, A. Pop, L. Scorus, R. Dudric, G. Stiufiuc, N. Vedeanu, R. Tetean, F. Loghin, R. Stiufiuc, C. M. Lucaciu, *Pharmaceutics* **2020**, *12*, 424.